A simple approach to the fabrication of mesoporous CuB_2O_4/CuS nanocomposite for robust photocatalytic and antibacterial activity

K. Rajasulochana[a], S.Selvarajan[b] , A.Suganthi[b,c]*, M.Rajarajan[d]

[a] Department of chemistry, Sri S.Ramasamy Naidu Memorial College, Sattur - 626203, Tamilnadu, India..

[b] P.G & Research Department of Chemistry, Thiagarajar College, Madurai 625 009, Tamil Nadu. India[b]

[c]Mother Teresa Women's University, Kodaikanal 624 102, Tamilnadu, India

[d]Madurai Kamaraj University, Madurai 625 021, Tamilnadu, India

Abstract: ***Novel $CuBi_2O_4$/CuS composite photocatalysts with different mass ratios 1%, 5%, 10% of $CuBi_2O_4$ have been synthesized by the solid-phase method and precipitation-deposition method.***

The physical and photophysical properties of the photocatalyst have been characterized by XRD, SEM, EDX, BET- surface area, UV-visible diffuse reflection spectra, photoluminescence spectra and Antibacterial activity. The prepared photocatalytic material of 10% $CuBi_2O_4$/CuS exhibited higher photocatalytic performance as well as excellent degradation of 4-Amino phenol (4-Ap) compared to the rest and the individual component. The results of PL indicated that $CuBi_2O_4$ and CuS could combine well to form a composite structure which facilitated electron-hole separation, and increasing photocatalytic activity. On the basis of the experimental results and estimated energy band positions, the mechanism of enhanced photocatalytic activity was proposed.

Keywords: ***$CuBi_2O_4$/CuS composites, UV-visible-light, 4-Aminophenol, Photocatalytic activity.***

1. Introduction

p-AP is the hydrolytic product of acetaminophen (paracetamol) and is reported to have significant nephrotoxicity and teratogenic effects, and has been detected as synthetic intermediate [1]. In view of p-AP, it is toxic, irritable to the eyes, skin and respiratory system. So it is released in the environment as a pollutant by the industrial activities. The common technologies explored for the remediation of p-AP are chemical precipitation, reverse osmosis, ion exchange, electrodialysis and adsorption. However, most of these techniques have their own limitations, effective only for the removal of heavy metals at trace level and the dealing costs are also relatively expensive. Besides the well-established methods, photocatalys is using semiconductor nanoparticles is an emerging technology for the degradation and mineralization of variety of organic pollutants (dyes, phenols, pesticides and pharmaceuticals) in aqueous media.

Semiconductor photocatalysts, which hold great potential for converting solar energy to chemical energy, have been proven to be available and promising materials for environmental purification [2].The key to the superior photocatalytic activity of semiconductor mainly lies in effectively combining the photon absorption, bulk diffusion and the separation of photo induced charge [3]. Unfortunately, the semiconductor oxides mostly have a wide band gap with relatively high recombination rate of electron-hole pairs, leading to a poor efficiency of photocatalytic reaction. Therefore, diverse approaches have been explored to enhance the quantum yield of semiconductors, including phase/morphological control, ion doping, surface sensitization, noble metal loading, and heterostructure constructing [4].

Recently, many investigations have been undertaken on the latter strategy. A great number of novel undoped single-phase mixed oxide semiconductor photocatalysts have been developed, such as $BiVO_4$ [5], $CuBi_2O_4$ [6], $PbBi_2Nb_2O_9$ [7] and so on. They all show certain absorption ability in the visible light range. One characteristic of these photocatalyst is their micro or submicro dimension. The larger sizes as compared to TiO_2 nanoparticles lead to higher density. So they show good precipitation performance and can easily be recovered in water purification. Yet they have some disadvantages such as small specific surface areas, long migration distance for excited electron-hole pairs, and increasing energy –wasteful recombination; all of these were expected to lower photocatalytic activities. It is reported that loading a small amount of noble metals or metal oxides, in particular, Pt, Au, Ag, NiO, and Fe_2O_4, [8-12] greatly improves the activity of these photocatalysts. However, some loading species can improve the photocatalytic performance, but other may debase it. It is determined by the energy band structures and morphologies characteristics of the loading species and photocatalysts. So designing more efficient and more readily separable visible-light-driven composites photocatalytic materials, which can meet the requirement of practical environmental application, is the goal of the researchers.

Semiconductors composite, some benefits can be realized: an improvement of charge separation, the lifetime of the charge carrier, and interfacial charge transfer efficiency, respectively [13]. For the above reason, it has attracted increasing attention in recent years. So far, variety semiconductor heterojunction including Bi_2O_3/ZrO_2, $BaTiO_3/Bi_2O_3$, $CuFe_2O_4/SnO_2$ [14–16] have been studied. Theoretically, two type of semiconductor is mutual sharing to each other to form micro p-n heterojunctions semiconductor and the inner electric field is produced in the interface. Some of the cases partially localized on structural defective centres of its crystalline lattice, hence improving the electrical properties of the semiconductor, because optical excitation, free electron (e^-), and electronic vacancy (a hole, h^+) are formed. $CuBi_2O_4$[17]has attracted sensitizer semiconductors due to its narrow bandgap 1.50 eV, and this excellent host matrix for luminescent active catalyst due to its low photon energy, high visible light active, thermal stability. Herein, we demonstrated the synthesis, characterization, and photocatalytic properties of

$CuBi_2O_4$/CuS nanocomposite under UV-visible-light-irradiation, and we discussed the mechanism of enhanced photocatalytic activity and antibacterial activity of this composite.

2. Experimental Section

Materials

All the chemicals used were of analytical grade and used as received without further purification

2.1. Synthesis of $CuBi_2O_4$

$CuBi_2O_4$ powder was prepared by solid-phase synthesis from the stoichiometric mixture of CuO and Bi_2O_3 [18] at 700℃ for 24 h in air.

2.2. Synthesis of $CuBi_2O_4$/CuS nanocomposite

The $CuBi_2O_4$/CuS nanocomposite was prepared by a precipitation-deposition method, with different ratios of $CuBi_2O_4$ was typically performed as follows. $CuBi_2O_4$ was added into 100 ml of deionized water completely by ultra-sonication, and then 10 ml of 0.15 M $Cu(NO_3)_3.5H_2O$ solution was added and this suspension was kept under magnetic stirring for 2 h. Subsequently, 20 ml of 0.10 M Na_2S solution was added drop by drop and kept stirring for 4h. Next, the products were recovered by filtration, washed by distilled water, and fully dried at 333K in an oven to obtain the final $CuBi_2O_4$/CuS nanocomposite with different weight addition ratios of $CuBi_2O_4$, namely, 1%$CuBi_2O_4$/CuS, 5% $CuBi_2O_4$/CuS and 10% $CuBi_2O_4$/CuS nanocomposite. For comparison, blank CuS was prepared using the same procedure in the absence of $CuBi_2O_4$.

2.3. Evaluation of the Photocatalytic Activity

Two types of reactions were employed for measuring the photoreactivity of the as-prepared powder: The photobleaching of water-organic pollutant, p-Aminophenol (p-AP), and the photocatalytic oxidation of terephthalic acid under UV-visible (268 nm) irradiation were carried out in a 250 ml cylindrical–immersion type photoreactor at room temperature in air and at neutral pH conditions. A suspension of the measured amount of photocatalyst and 200 mL of an aqueous solution of p-AP was magnetically stirred for 3 hrs or more before irradiation to establish an adsorption-desorption equilibrium. The reactor was then irradiated by a 150 W A. The light intensity was fixed on 70mW/cm^2 when the reactor was placed 10 cm away from the light source mirror. At specific time intervals, 4 ml suspensions were sampled and centrifuged at 5000 rpm for 10 min to remove the photocatalyst. The concentration of remnant p-AP solution after irradiation was analyzed with a UV-visible-spectrometer (JASCO – VB –5040) by recording the absorption band maximum at 268 nm. Chemical oxygen demand (COD) experiments were performed by the dichromate oxidation method [14], after the completion of photodegradation. The degradation efficiency (DE) of each catalyst was computed using the following equation.

$$DE = 100\ \%*(C_0-C) / C_0 \quad (1)$$

Where C is the concentration of p-AP at the time interval t and C_0 is the concentration after the adsorption equilibrium is reached before irradiation.

A fluorescence spectrum of 2-hydroxy terephthalic acid was measured on a fluorescence spectrophotometer (JASCO-FP-6200). The $OH^{\bullet}$ radical trapping experiments were carried out using the following procedure: terephthalic acid (TA) (16.6 mg/L) was first dissolved in 200 mL of dilute 0.2M NaOH solution, followed by the addition of 100 mg of photocatalyst. The suspension was irradiated by a 150 W tungsten lamp at the wavelength in the range of 300–740 nm for 180 min. The fluorescence emission spectrum of the solution was measured for every 30 min illumination [19]. Recycling experiments were performed as follows: after each cycle, the catalyst was separated by centrifugation, washed thoroughly with distilled water, and added to a fresh p-AP aqueous solution.

2.4. Characterization

X-ray powder diffraction (XRD) analysis was carried out on a Bruker D8 Diffractrometer with high-intensity Cu-Kα (λ = 1.54 A°). UV-Vis diffuse reflectance spectroscopy was recorded on an UV-2450 spectrophotometer (Shimadzu Corporation, Japan) using $BaSO_4$ as the reference. The structural information of the samples was measured by PL spectra were recorded with a Perkin-Elmer (LS-45)) fluorescence spectrophotometer. The PL spectra were measured at room temperature under excitation at 350 nm provided by emission from a xenon lamp. Scanning electron microscopy (SEM) observations were performed by means of a JSM 6701F-6701 instrument in both secondary and backscattered electron modes. The elemental analysis was detected by an energy dispersive X- ray spectroscopy (EDX) attached to the SEM. The BET surface area was derived from the N_2 adsorption – desorption isotherm by the Barrer-Joyner-Halenda (BJH) technique. Photodegradation experiments were performed in a HEBER immersion type photoreactor.

3. Results and discussion

3.1. Optical absorption properties

Fig.1 displayed the UV-vis DRS of $CuBi_2O_3$/CuS nanocomposite and bare $CuBi_2O_4$, CuS nanoparticles. An intense UV absorption band appears from 200 nm to 510 nm, which ascribed the electrons promotion of $CuBi_2O_4$ from the valence band to the conduction band. It was interesting to observe that the $CuBi_2O_4$/CuS nanocomposite possess much better UV-visible light absorption intensity than TiO_2, which was consistent with the colour of the samples indicating that they may have higher photocatalytic activity for a target reaction under UV-visible light irradiation, especially the 10% $CuBi_2O_4$/CuS ones. In contrast to the prepared $CuBi_2O_4$, the absorption edge of the $CuBi_2O_4$/CuS nanocomposite

displays different shifts to the UV-visible light region. This was confirmed by estimating the energy bandgap of the samples according to the plot are shown in Fig.2 (a-e). The band gap energy of a semiconductor could be calculated by following the equation [20].

$$\alpha h\nu = A\,(h\nu - E_g)^{n/2} \qquad (2)$$

Here, α, ν, E_g, and A are the absorption coefficient, light frequency, band gap energy, and a proportionality constant, respectively. Among them, n decides the kind of optical transition in a semiconductor. The band gap energies of the $CuBi_2O_4$ and CuS samples can be estimated from the plots of $(\alpha h\nu)^2$ versus photon energy (hν) and $(\alpha h\nu)^{1/2}$respectively. The intercept of the tangent to the X-axis would give a good approximation of the band gap energies for the synthesized products are displayed. The band gap estimated energies of the resulting samples were about 1.45 eV, 2.32 eV, 3.32 eV, 3.09 eV, and 3.18 eV for $CuBi_2O_4$, CuS, 1% $CuBi_2O_4$, 5% $CuBi_2O_4$, and 10% $CuBi_2O_4$/CuS nanocomposites, respectively.

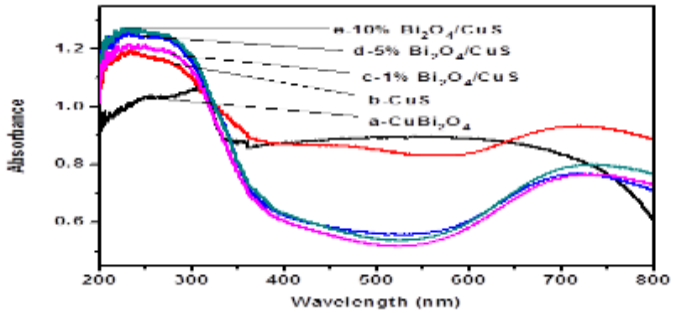

Fig.1. UV-Vis DR spectra of (a) $CuBi_2O_4$ (b) CuS(c) 1% $CuBi_2O_4$/CuS (d) 5% $CuBi_2O_4$/CuS (e) 10%$CuBi_2O_4$/CuS composite.

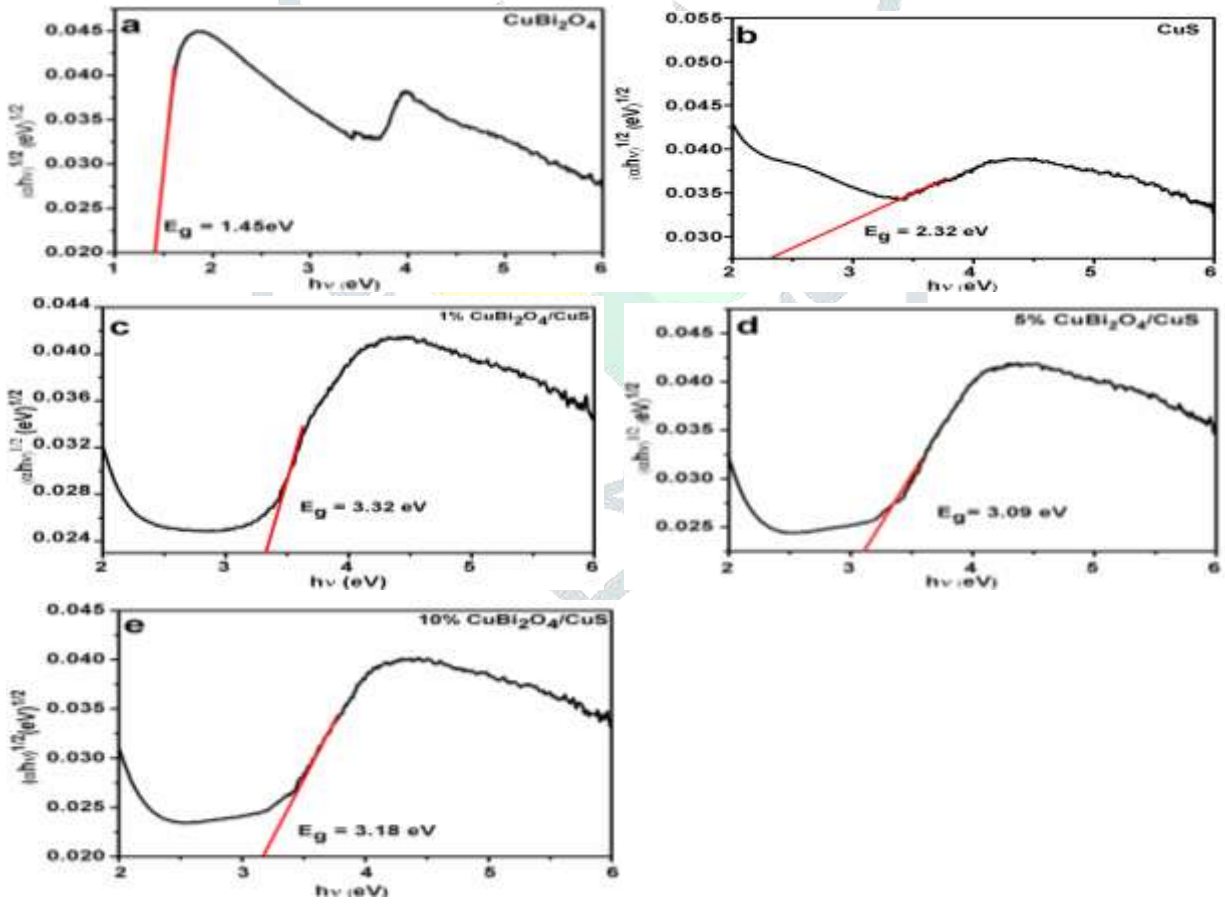

Fig.2. Tauc plot of $(\alpha h\nu)^{1/2}$ vs photon energy (hν) for the band gap energy of (a) $CuBi_2O_4$ (b) CuS (c)1% $CuBi_2O_4$/CuS (d) 5% $CuBi_2O_4$/CuS and (e) 10% $CuBi_2O_4$/CuS nanocomposite.

3.2 FT-IR analysis

The structural information of $CuBi_2O_4$, CuS and 10% $CuBi_2O_4$/CuS nanocomposite are confirmed by FTIR spectroscopy and displayed in Fig.2. The FTIR spectrum of $CuBi_2O_4$ (Fig.3a) shows a broad band at 400–900 $cm^{-1}$are mainly related to Bi – O, Cu – O, Cu-S

stretching and Cu – O – Cu (M – O – M, (M = Cu, Bi) bridging stretching modes, which can reflect the variation of structure in crystal. The band at 3532 cm^{-1} showing there are more hydroxyl groups on the surface of $CuBi_2O_4$/CuS nanocomposite [21, 22]. In the FTIR spectrum of CuS (Fig.3 curve b), absorption band below at 600 $cm^{-1}$is attributed to Cu–S stretching vibration mode and a band at 1631 $cm^{-1}$is ascribed the O–H bending vibration of adsorbed water molecules. The FTIR spectrum of the 10% $CuBi_2O_4$/CuS (Fig.3 curve c) exhibits the characteristic peak of CuS at 1626 cm^{-1} is shifted to 1648 cm^{-1} corresponded to the formation of composition of $CuBi_2O_4$/CuS nanocomposite. Therefore, the prepared $CuBi_2O_4$ was successfully decorated with CuS nanoparticles.

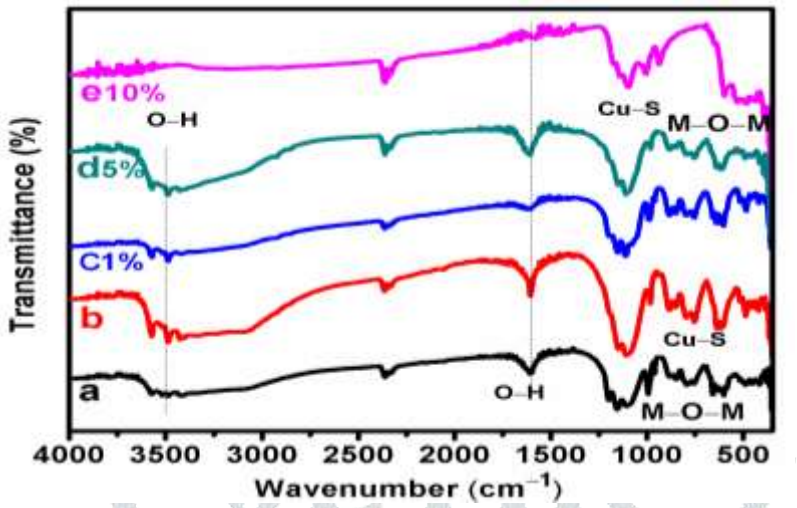

Fig.3. FTIR spectrum of (a) $CuBi_2O_4$ (b) CuS(c) 1% $CuBi_2O_4$/CuS (d) 5% $CuBi_2O_4$/CuS (e) 10% $CuBi_2O_4$/CuS micromotors nanocomposite.

3.3. XRD Analysis.

The crystal structures of the prepared material were investigated by the XRD method, and the results were displayed in Fig.4. The results shows that the diffraction peaks of the pure $CuBi_2O_4$ sample and pure CuS sample were in good agreement with the tetragonal phase of $CuBi_2O_4$ (JCPDS card no, 42–0334) and the hexagonal phase of CuS (JCPDS card no,74–1234), respectively. For the $CuBi_2O_4$/CuS nanocomposite, all the $CuBi_2O_4$ diffraction peaks were found at $CuBi_2O_4$/CuS nanocomposite. With the increase of $CuBi_2O_4$, the diffraction peaks intensity of $CuBi_2O_4$ become stronger, while the characteristic peaks of CuS decrease in intensity. The characteristic peaks of CuS (18.56°) intensity decreased when the $CuBi_2O_4$ content was more than 5% .While the $CuBi_2O_4$ content was increased to 10%, the characteristic peaks of CuS (15.04°) disappeared. This may be due to the better crystallinity of $CuBi_2O_4$ materials, and some of the characteristic peaks of CuS coincide with that of $CuBi_2O_4$. This result suggests that $CuBi_2O_4$ and CuS coupled together successfully. Additionally, the peaks of the $CuBi_2O_4$/CuS composites were broad, which seems to be that the particles of the samples were quite small. The average crystalline size of the obtained samples was computed by scherrer formula [21].

$$D = k\lambda / \beta\cos\theta \qquad (1)$$

Here, D is the crystallite size, k is correction factor, which is taken as 0.9, β is the full width at half-maximum (FWHM) of the most intense diffraction peak of 220 plane of $CuBi_2O_4$ and 004 plane of CuS, respectively. The λ is the wavelength of Cu target (1.5406A°), and θ is the Bragg diffraction angle. The average crystalline size of pure $CuBi_2O_4$, CuS, 1% $CuBi_2O_4$/CuS, 5% $CuBi_2O_4$/CuS, and 10% $CuBi_2O_2$/CuS nanocomposite was found to be 33.28 nm, 31.85 nm, 34.67 nm, 39.12 nm, and 41.98 nm, respectively.

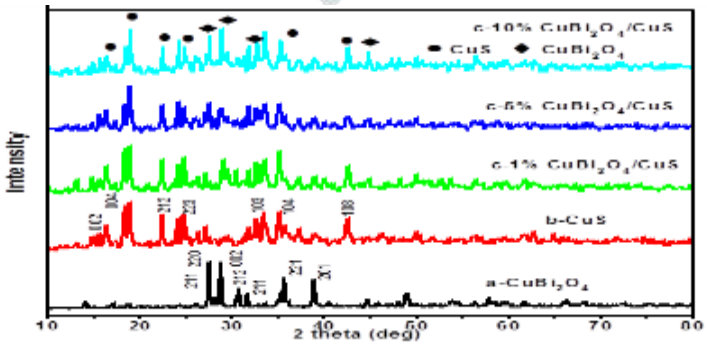

Fig.4. X-ray diffraction patterns of (a) $CuBi_2O_4$ (b) CuS(c) 1% $CuBi_2O_4$/CuS (d) 5% $CuBi_2O_4$/CuS (e) 10% $CuBi_2O_4$/CuS nanocomposites.

3.3 Photoluminescence Spectra analysis

During the photocatalytic process, the charge transfer and recombination are combinations of two competitive reaction pathways, so it was important to suppress the recombination rates and accelerate charge transfer to produce more hydroxyl radicals, which were directly beneficial for the oxidation of pollutants. To investigate the efficiency of charge carrier trapping, immigration, and transfer in the as-prepared $CuBi_2O_4$ and CuS, we measured their photoluminescence (PL) emission spectra and are shown in Fig 5. The broad PL emission spectrum was measured for pure $CuBi_2O_4$, which could be attributed to the irradiative recombination process of self-trapped excitations. The photoluminescence spectra of the prepared (a) $CuBi_2O_4$, (b) CuS , and (c)10% $CuBi_2O_4$/CuS with an excitation wavelength of 380 nm. It was found that PL emission intensity of the 10% $CuBi_2O_4$/CuS composite was dramatically weakened compared with that of bare $CuBi_2O_4$ and CuS which clearly indicates that the recombination of photogenerated charge carriers was greatly restrained by the coupling of $CuBi_2O_4$ and CuS. In other words, the separation efficiency of photogenerated electrons and holes in 10% $CuBi_2O_4$/CuS was higher than those in the bare $CuBi_2O_4$ and CuS. It can be inferred that the prepared 10% $CuBi_2O_4$/CuS nanocomposite having a higher photocatalytic activity than bare $CuBi_2O_4$ and CuS.

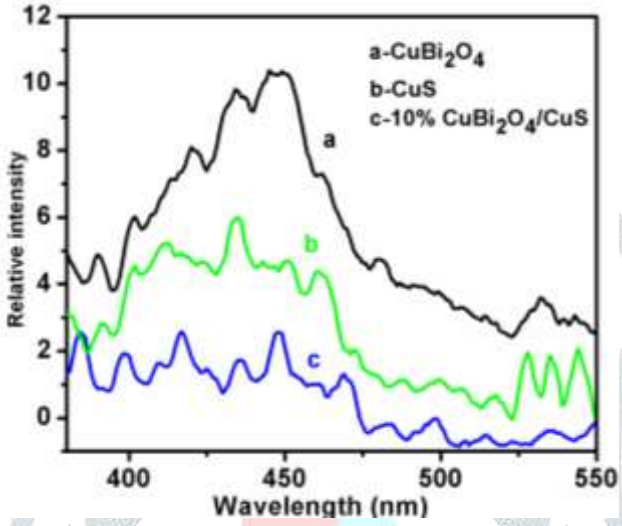

Fig.5. PL spectra of (a) $CuBi_2O_4$, (b) CuS, (c) 10% $CuBi_2O_4$/CuS nanocomposite.

3.5 Mesoporous properties

The surface area of the 10% $CuBi_2O_4$/CuS nanocomposite was investigated by nitrogen adsorption-desorption isotherms [24, 25] and pore size distribution (inset) was shown in Fig 6. This N_2 adsorption -desorption isotherm could be identified as a typical type IV, indicating that the as-prepared composites were mesoporous materials because the single point adsorption P/P_0 (0.9936 is 0.054 cm $^{-3}$ g $^{-1}$) was related to the pore size. The pore size distribution statistics designate that the majority of the pores are 137 A°. These pores seemingly arise from the spaces among nanosheets inside the 10% $CuBi_2O_4$/CuS microspheres. The BET surface area was 33.76 m^2 g^{-1}. The BET surface area and large total pore volume strongly indicates that the as-prepared microspheres have a mesoporous structure.

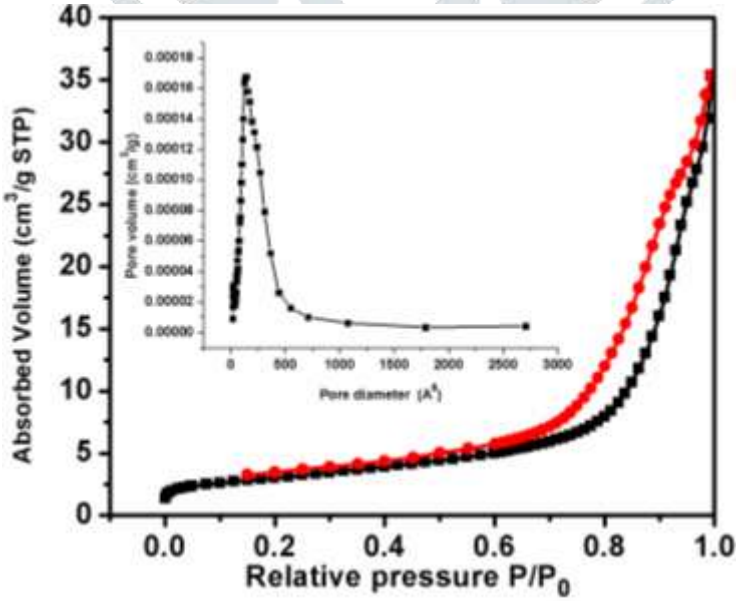

Fig.6. N_2 adsorption-desorption isotherm and Barrett – Joyner – Halenda (BJH) pore size distribution plot (inset) of 10 % $CuBi_2O_4$/CuS micromotors nanocomposite.

3.6 Surface morphology and microstructure

The detailed morphology and particles size of the pure $CuBi_2O_4$, CuS, and 10% $CuBi_2O_4$/CuS composites were inspected by scanning electron microscopy. Fig. 7 presented the surface view of SEM images of pure $CuBi_2O_4$, CuS, and 10% $CuBi_2O_4$/CuS nanocomposite. The morphology of the pure $CuBi_2O_4$ appeared as shapeless sheet aggregates with size ranging between 25 and 45 nm (Fig. 7a). The pure CuS (Fig.7b) consists of large rice-like grain and rod shape particles with size ranging from 45 nm to 55 nm. Fig.7b shows a surface morphology of 10% $CuBi_2O_4$/CuS is clearly expressed loosely sphere like (indicated in red ring mark) structure with size range from 20 nm to 30 nm. The chemical composition of the nanocomposite was further determined by the energy dispersive X-ray spectroscopy (EDAX), and it clearly conforms to the presence of Cu, Bi, O, and S elements, as shown in Fig. 7 d.

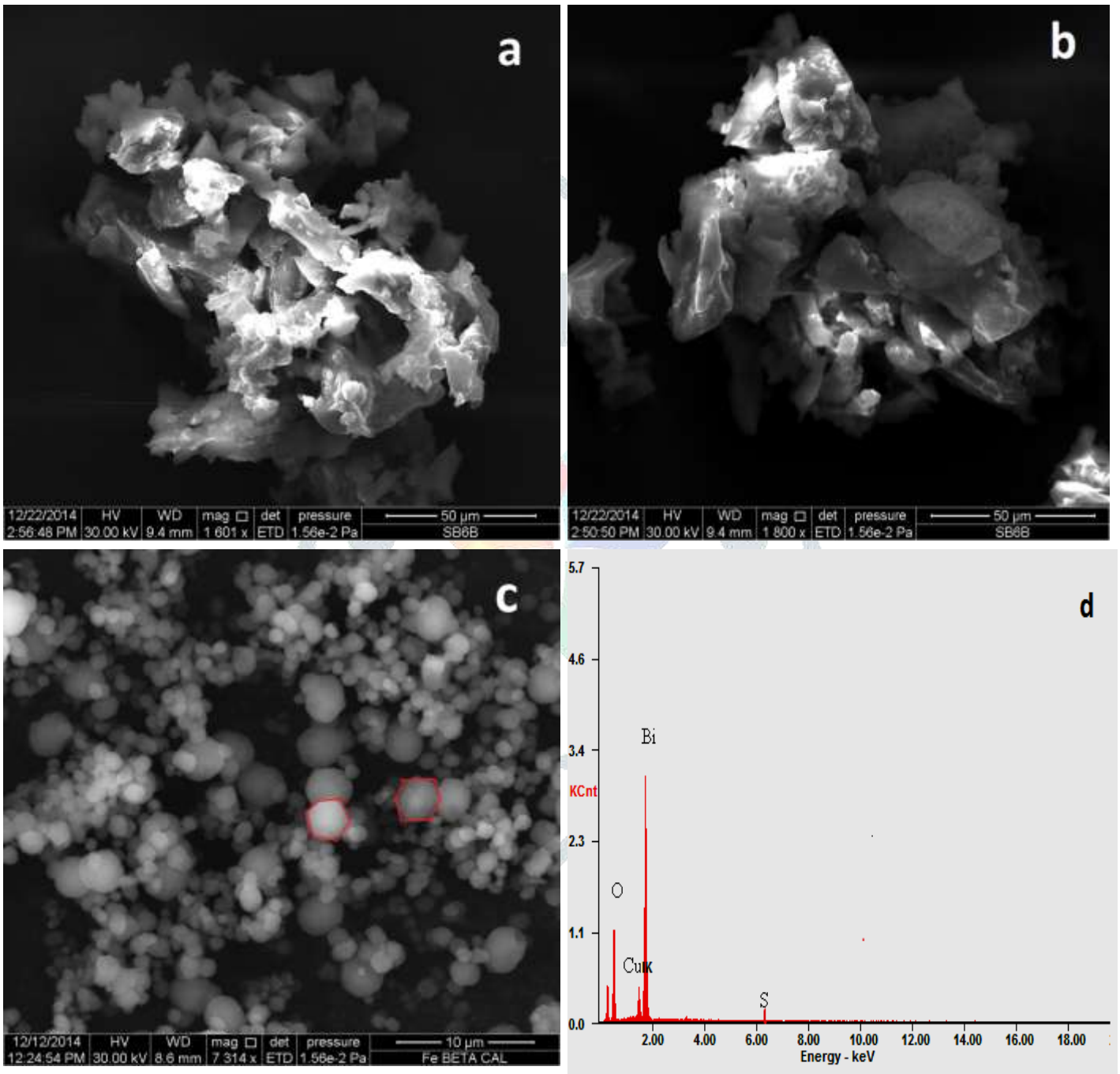

Fig.7. SEM image of (a) $CuBi_2O_4$ (b) CuS (c) 10%$CuBi_2O_4$/CuS (d) EDAX pattern of 10% $CuBi_2O_4$/CuS nanocomposite.

The surface morphology and particle size of 10% $CuBi_2O_4$/CuS nanocomposite was further characterized by TEM which showed the direct information about the distribution of the metal oxides on the nanocomposite surface. Fig.8 a shows that several particles have spherical like shape with particle size about 20 nm. The bright gray and black color spherical agglomerates are obviously due to the presence of $CuBi_2O_4$ and CuS, which is in good agreement with the XRD results. This result indicates that the presence of the CuS has

affected the shape and size of the nanomaterials. The selected area electron diffraction (SAED) pattern of the 10% $CuBi_2O_4$/CuS nanocomposite is represented in Fig.8 (b). The SAED pattern of the 10% $CuBi_2O_4$/CuS nanocomposite displayed the tetragonal phase of CuB_2O_4 and hexagonal phase of CuS which coincides well with the XRD pattern. The brighter inner ring corresponded to (100), (101) and (111) plane of the tetragonal phase of $CuBi_2O_4$, and the light spots corresponding to the (110), (101) and (211) planes of the tetragonal phase of $CuBi_2O_4$. The bright ring pattern shows the polycrystalline nature of $CuBi_2O_4$, and the bright spots without rings confirm the single crystalline nature of CuS. The SAED patterns of the 10% $CuBi_2O_4$/CuS nanocomposite confirm that the product is well crystallized [26, 27].

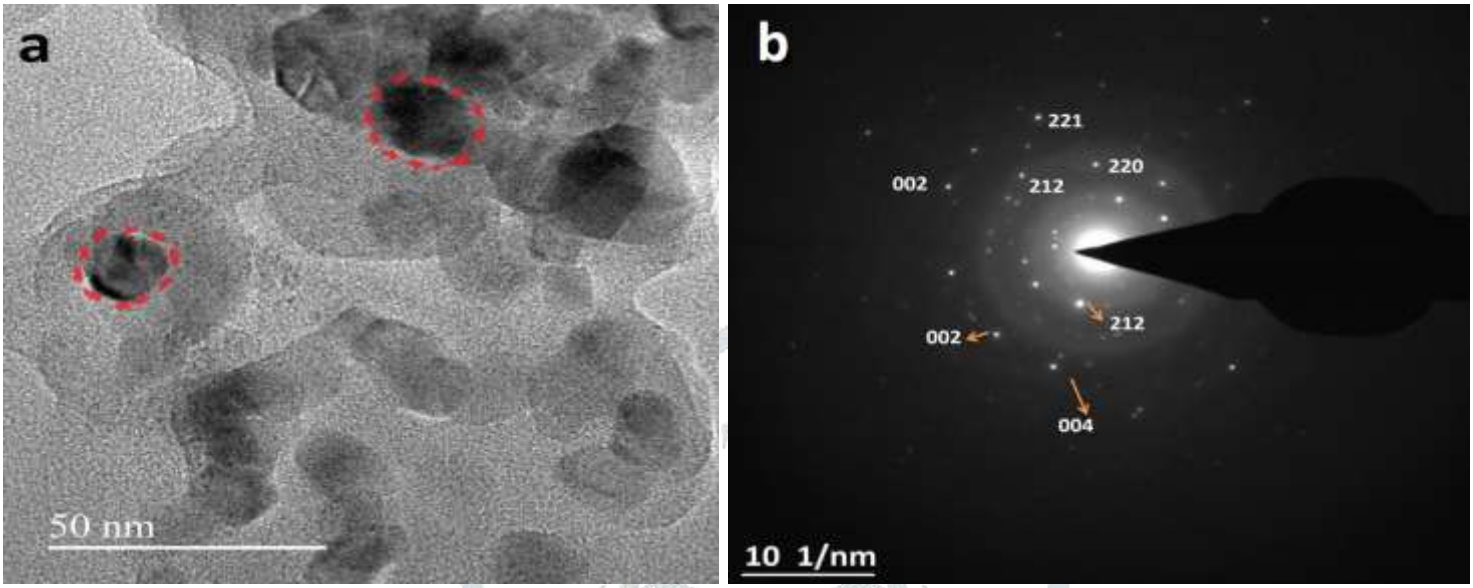

Fig.8.TEM and SAED pattern of 10% $CuBi_2O_4$/CuS micromotors nanocomposite.

3.7 Photocatalytic performance

The semiconducting materials absorb photons with energy greater than that of the band gap energy, excite electrons from valence band to conduction band, and leave holes in the valence band. The photogenerated electron – hole pair in the bulk materials are separated and then move to the photocatalyst surface without recombination. The electron – hole pair present on the surface of the materials react with the surface adsorbed species and produce degradation products. In order to compare the photocatalytic activity of bare $CuBi_2O_4$, CuS and $CuBi_2O_4$/CuS with different $CuBi_2O_4$ contents, photodegradation experiments were carried out by using p-AP as a target pollutant under UV- visible-light irradiation (λ_{max} = 268 nm). The photocatalytic reactions of the prepared samples were performed under three different conditions: (1) Degradation of the p-AP was monitored under UV-visible-light for 3 h without using photocatalysts. From this experiment, it was observed that the concentration of p-AP hardly decomposed under UV-visible-light irradiation in the absence of the photocatalyst. (2) The control experiments were performed for 30 min under the dark condition in presence of photocatalysts, which indicated the adsorption of p-AP on the active sites of the photocatalyst. (3) Lastly, the degradation of p-AP was monitored in the presence of all the photocatalysts and UV-visible-light. The temporal UV-visible-absorption spectral changes during the photocatalytic degradation of p-AP in aqueous solution in the presence of 10% $CuBi_2O_4$/CuS was represented in Fig 9a. An evident decrease in p-AP absorption at λ = 268 nm was observed that, accompanied by a shift in the absorption band towards the red region. After the irradiation for 180 min, both the maximum absorption peak and absorption at λ_{max} was disappeared, which indicates that p-AP could be completely degraded by using 10% at $CuBi_2O_4$/CuS.

The percentage of p-AP degradation over all the photocatalysts as a function of the exposure time were represented in Fig 9b. The percentage of degradation of p-AP over all the photocatalysts follows the following order: 10% $CuBi_2O_4$/CuS > 5% $CuBi_2O_4$/CuS > 1% $CuBi_2O_4$/CuS > $CuBi_2O_4$> CuS. Therefore, the critical molar proportion of $CuBi_2O_4$ to CuS was found to be10% which exhibits the best photocatalytic activity toward degradation of p-AP over all the photocatalyst. The said photocatalyst was able to degrade 84.4% of p-AP solution in 3h under UV-visible-light irradiation.

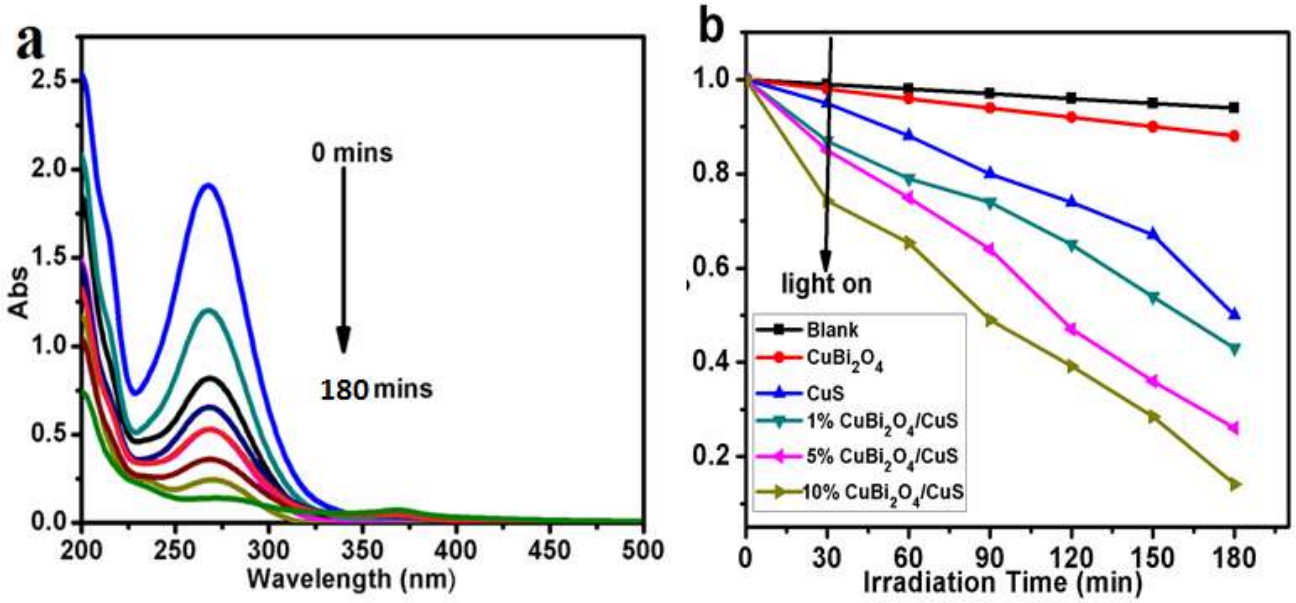

Fig.9.(a) Time-dependent visible absorption spectra of the p-AP in the presence of 10% $CuBi_2O_4$/CuS micromotors nanocomposite under visible light irradiation (λ_{max} = 246 nm) time using photocatalysts (b) Degradation rates of p-AP UV-visible light irradiation without catalyst and in the presence of $CuBi_2O_4$, CuS and $CuBi_2O_4$/CuS samples.

3.7.1. Possible Photocatalysis Mechanism

The photocatalytic mechanisms of $CuBi_2O_4$/CuS nanocomposite were represented in Fig.10. The band-edge potential levels of two semiconductors play a crucial role in determining the flowchart of photoexcited charge carrier in the coupled semiconductors. The valence band (VB) edge and the conduction band (CB) edge positions of $CuBi_2O_4$/CuS can be calculated from the following empirical formula [27, 28].

$$E_{VB} = X - E_e - 0.5E_g \quad (3)$$

$$E_{CB} = E_{VB} - E_g \quad (4)$$

Where X is the absolute electronegative of the semiconductor; expressed as the geometric mean of the absolute electronegativity of the constituent atoms, which is defined as the arithmetic mean of the atomic electron affinity and the first ionization energy; E_{VB} is the valence band edge potentials, E_{CB} is the conduction band edge, E_g is the band gap energy of the semiconductor, E_e is the energy of free electrons on the hydrogen scale (~ 4.5 eV). The predicted band edge positions of $CuBi_2O_4$ and CuS by the above equation are shown in Table 1.

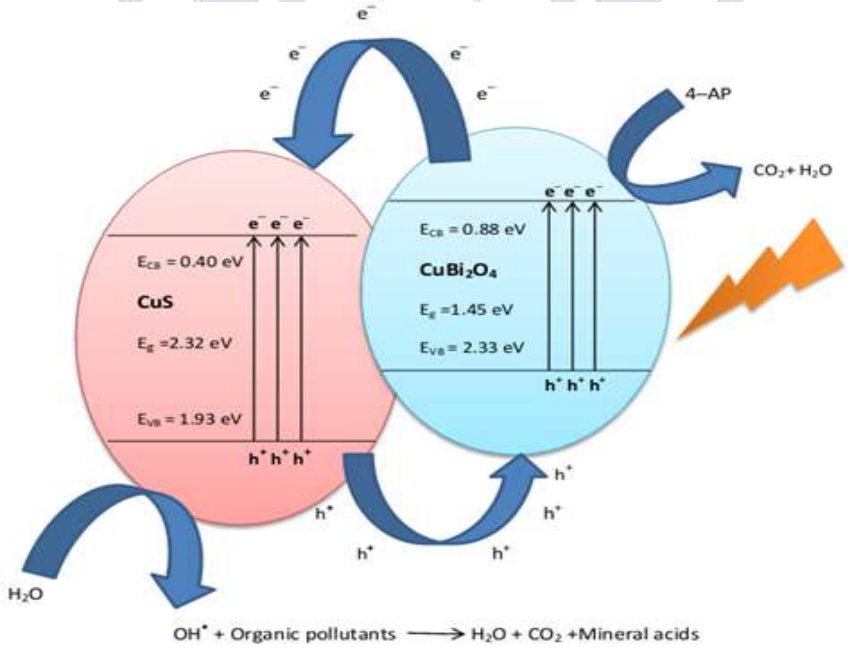

Fig.10. Schematic illustration of the charge transfer pathways during p-AP degradation process over$CuBi_2O_4$/CuS micromotors under UV-visible light irradiation.

Table 1. Absolute Electronegativity, Estimated Band GAP, Energy levels of the calculated Conduction band Edge, andValence band edges for $CuBi_2O_4$/CuS composite.

Semiconductor Oxide	Absolute electronegativity (X)	Estimated energy band gap E_g (eV)	Calculated conduction band edge (eV)	CalculatedValence band edge (eV)

Both $CuBi_2O_4$ and CuS could be easily excited under UV-visible light irradiation and the corresponding photoinduced electron-hole pair are generated. Due to the CB edge potential of CuS(0.40 eV) being more negative than that of $CuBi_2O_4$ (0.88 eV), and VB of $CuBi_2O_4$ (2.33 eV) being more positive than that of CuS (1.93 eV), the local electric field at the $CuBi_2O_4$/CuS nanocomposite interface pushes the photogenerated electrons toward the CB of $CuBi_2O_4$, and holes on the of $CuBi_2O_4$ migrate to that of CuS at the same time. This band offset could lead to the retardation of the photogenerated electron−hole recombination rate. In such a way, the photogenerated electrons can be effectively collected by $CuBi_2O_4$ and holes can be effectively collected by CuS. Therefore, the efficient separation of photogenerated electrons and holes can be achieved, and the recombination process of electrons−hole pairs can be hindered, in accordance with the result of the PL. Therefore, the $CuBi_2O_4$/CuS micromotorsnanocomposite exhibits enhanced performance as compared to bare $CuBi_2O_4$ and CuS.

The effect of radicals scavenger on the rate of the photodegradation of p-AP under UV-visible light irradiation, over 10% $CuBi_2O_4$/CuS nanocomposite was examined in order to further make the reaction mechanism clear. To investigate the presence of $OH^{\bullet}$ radicals, we used terephthalic acid (TA) as fluorescent properties. The $OH^{\bullet}$ radical was known to be trapped by the TA to produce the fluorescent 2-hydroxyterephthalic acid [19]. This result was displayed in Fig. 11which indicates the gradual increase in the fluorescence intensity at 410 nm was observed with increasing illumination time. The generated spectrum has the identical shape and maximum wavelength with that of 2-hydroxy terephthalic acid, indicating that the $OH^{\bullet}$ radical was indeed formed.

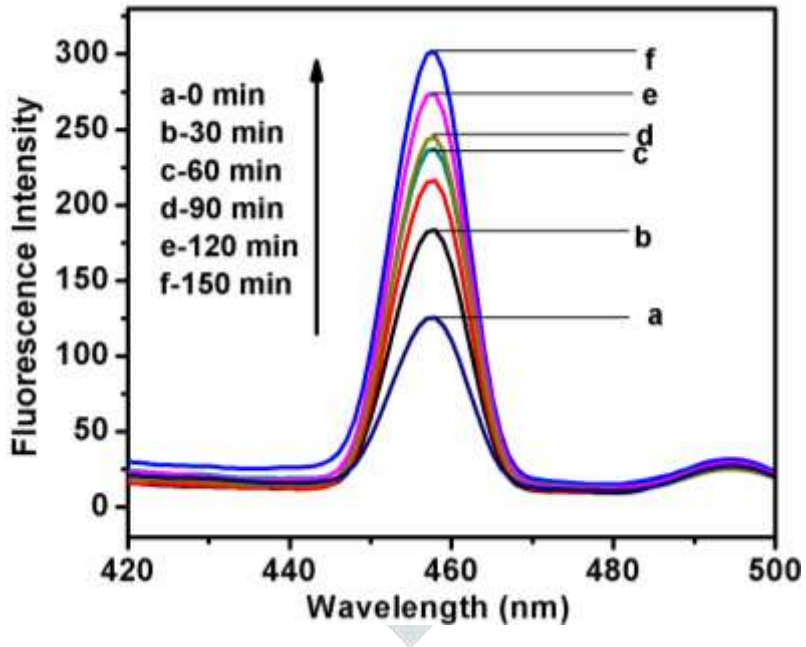

Fig.11. $^{\bullet}$OH –trapping fluorescence spectra of 10% $CuBi_2O_4$/CuS in a 16 mg/L basic solution of terephthalic acid.

3.7.2. Effect of pH

The pH of the solution was one of the most important parameters in the photocatalytic degradation of p-AP was studied using the initial concentration of 15µM, and semiconductors metal oxide loading of 350 mg/L. It determines the surface charge properties of the photocatalyst and performance towards the organic pollutants. Fig. 12 shows the difference of the apparent rate constant of the photodegradation by varying the initial pH of the aqueous solution from 2 to 10. The pH was adjusted using NaOH in the case of alkaline solutions and using H_2SO_4 in the case of acetic solutions. Photocatalytic activity reached a maximum near the zero point charge (pH_{pzc}=6), followed by a decrease of the apparent rate constant in the alkaline conditions. This results indicated that the degradation apparent rate constant decreased with an increased pH from 6 to10, increase until the optimum (pH=6) and then decrease in alkaline medium. The pH influences the adsorption of organic pollutants molecules on 10% $CuBi_2O_4$/CuS nanocomposite surface, which is an important period in photodegradation [29]. It can be assumed that for pH_{pzc}, the positive excess charge at the catalyst surface due to the surface adsorption of H^+ ions favours the approach of anionic species to the catalyst surface, whereas for higher pH excess of absorbed OH^- ions has the cationic species.

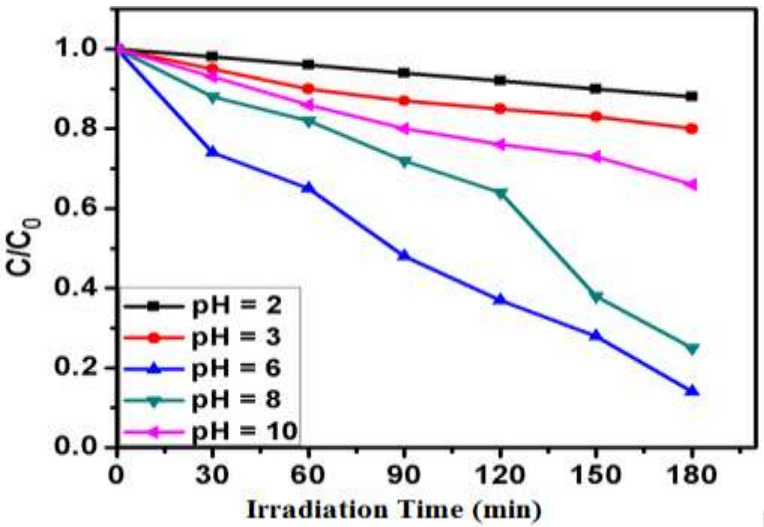

Fig.12. Effect of pH.

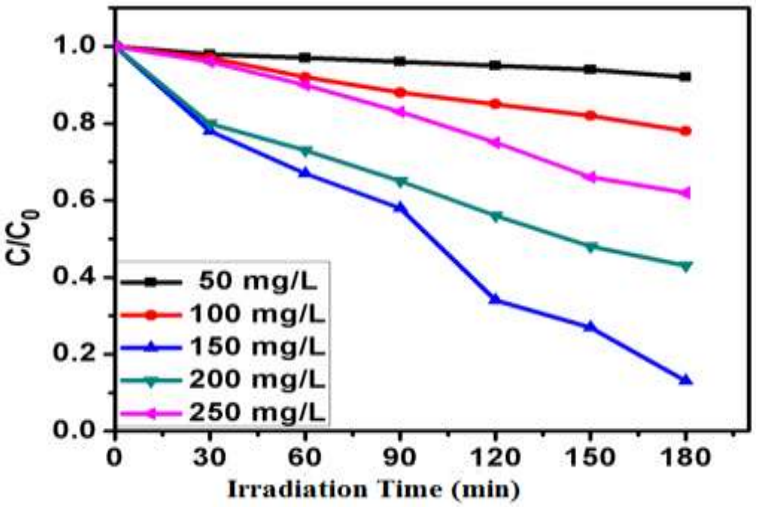

Fig.13. Effect of catalyst dosage.

3.7.3 Effect of catalyst

The influence of the photocatalyst concentration on the degradation and mineralization of p-AP was investigated using 10%$CuBi_2O_4$/CuS (50mg/L to 750 mg/L). Fig 13shows the p-AP photodegradation. 10%$CuBi_2O_4$/CuS exhibit superior activity when the amount of catalyst in the vessel increased up to 350 mg/L and then decreased. Whether in static, dynamic flow reactor, the initial reaction rates were established to be directly proportional to catalyst dosage indicating a heterogeneous regime. The lower catalyst loading much of light may be transmitted through the solution and higher amount of catalyst loading may be explained in term of complete ingesting of incident photons remarkable on the availability of active sites at the catalyst surface i.e., higher adsorption of incident light can be lead to the formation of high photoactivated volume in suspension thereby increasing the efficiency of the system [30]. However, it has been observed that above a certain concentration, the reaction rate levels off and independent of the catalyst dosage.

3.7.4. Effect of concentration

The influence of initial p-AP concentration on its photodegradation investigated in the presence of 350 mg/L of 10% $CuBi_2O_4$/CuS nanocomposite at pH 6 and varying p-AP concentrations from 5 to 25 µM and the results are displayed in Fig.14. The photodegradation of p-AP decreases with increases of p-AP concentration from 15 to 25 µM. This is due to the following reasons: At high pollutants concentration, the generation of reactive species on the photocatalyst surface is reduced because the active sites are completely covered by the pollutants molecules. According to Beer–Lamberts law the path length of photons entering into the pollutants solution decreases. The generation of reactive species also remains constant at a fixed catalyst concentration [31].

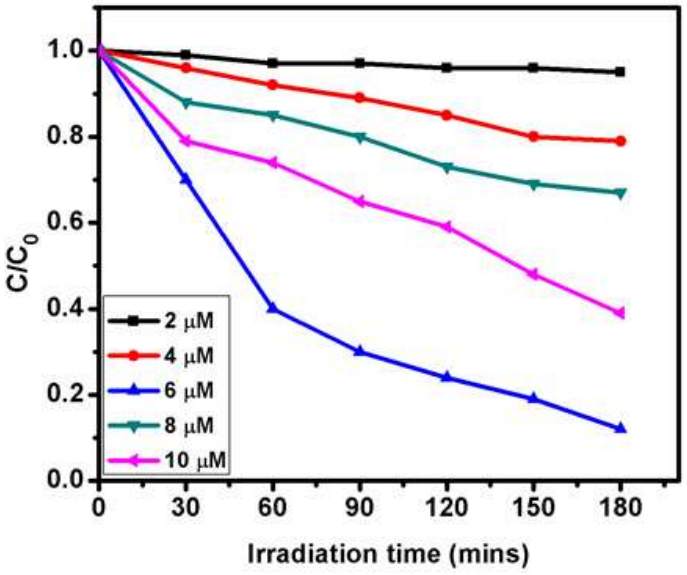

Fig.14. Effect of concentration.

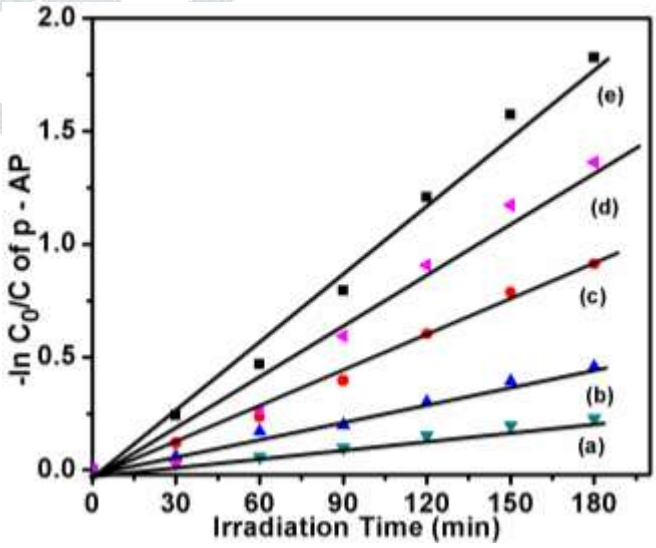

Fig.15. Kinetics of photodegradation of p-AP by using $CuBi_2O_4$,CuS and $CuBi_2O_4$/CuS nanocomposite with different mass ratio under UV-visible light (λ_{ma} =268nm).

3.8. Kinetics of photocatalytic degradation of p-AP

The kinetics of p-AP degradation under visible light overall photocatalyst was investigated by applying the Langumiur –Hindhelwood model [32].

$$-\ln (C_0/C) = kt \quad (5)$$

Here, k is the pseudo-first-order rate constant. The plots ln (C_0/C) versus irradiation time (where C_0 is the initial concentration of the p-AP and C is the concentration of the p-AP in the reaction time) were found to be linear as shown in Fig 15, and this suggests that photodegradation reaction follow pseudo-first-order kinetics. The apparent reaction rate constant (k) for the photocatalytic degradation of p-AP were evaluated from experimental data using a linear regression. In all case, the R^2 (correlation coefficient) value was greater than 0.99, which confirmed the proposed rate law for p-AP degradation. The apparent rate constant for $CuBi_2O_4$, CuS, 1% $CuBi_2O_4$/CuS, 5% $CuBi_2O_4$/CuS, 10 % $CuBi_2O_4$ were determined as 0.0004, 0.0008, 0.0012, 0.0047, 0.0087, and 0.0094 min^{-1}, respectively. The decreasing order of rate constants is summarized as follows: 10% $CuBi_2O_4$/CuS > 5% $CuBi_2O_4$/CuS > 1% $CuBi_2O_4$/CuS > $CuBi_2O_4$ > CuS. The corresponding k values of $CuBi_2O_4$/CuS nanocomposite were much higher than that of $CuBi_2O_4$ and CuS. Especially, 10% $CuBi_2O_4$/CuS exhibited the highest k value. From the above degradation results, we conclude that all the $CuBi_2O_4$/CuS composites exhibit much higher photocatalytic activities than that of single phase $CuBi_2O_2$ and CuS.

COD (carbon oxygen demand) and TOC (total oxygen demand) measurements were carried out under optimum reaction conditions (p-AP concentration 5 mM, catalyst concentration 0.75 0 g/L, pH 4 and irradiation time 180 min) to estimate the toxicity of the photodegraded pollutants solutions and the results are shown in Fig. 16.As can be seen that, the solutions obtained after photodegradation showed significant removal in COD (74%) and TOC (68 %). These results suggested that most of the p-AP pollutant molecules are mineralized under the photodegradation process.

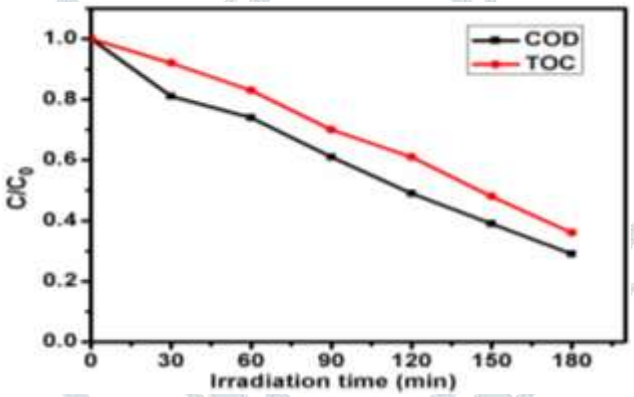

Fig.16 Plots of COD and TOC removal efficiency vs, irradiation time. Experimental conditions: [p-AP= pH 6, catalyst dosage 350 mg/L, concentration 15 µM]

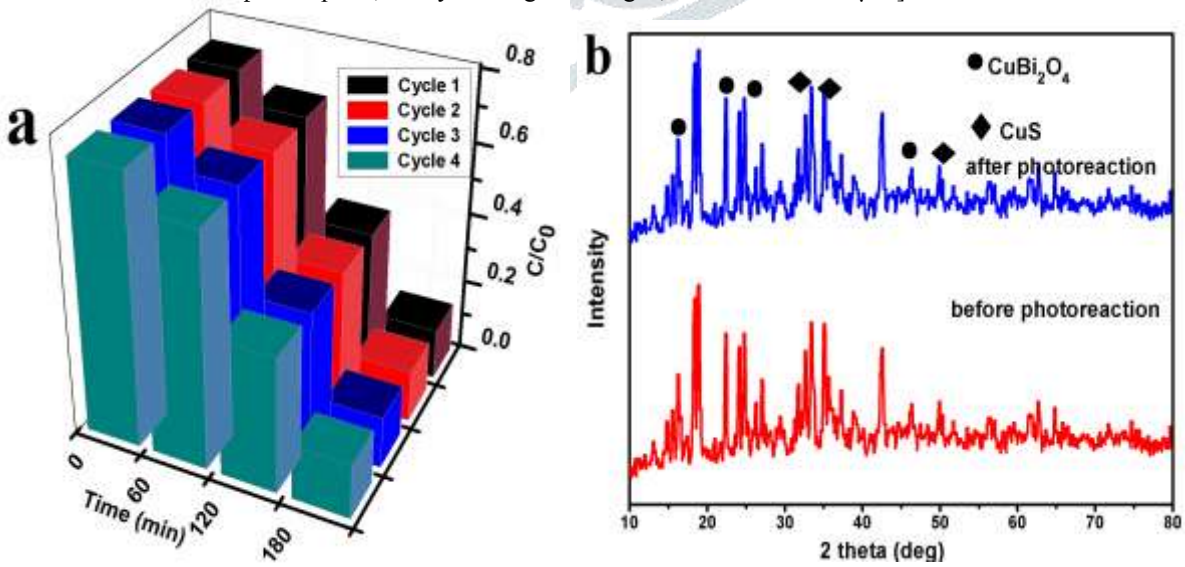

Fig.17a. Recycling tests of 10% $CuBi_2O_4$/CuS under simulated visible light irradiation. **b.**XRD patterns of 10% $CuBi_2O_4$/CuS before and after photoreaction.

3.10. Reusability of the Catalyst

The recycle experiment of the $CuBi_2O_4$/CuS micromotorsnanocomposite for photocatalytic reaction under simulated UV-visible light was investigated to evaluate the optical stability of the catalyst and the results are shown in Fig 17. The 10% $CuBi_2O_4$/CuS nanocomposite did not exhibit significant loss of photocatalytic performance after four runs, and about 84.4% of p-AP could be degraded after four runs(Fig.17a). The reports indicate that 10% $CuBi_2O_4$/CuS keep its photocatalytic efficiency performance without distinct photocorrosion during the oxidation of pollutant. In addition, the XRD pattern of the 10% $CuBi_2O_4$/CuS after four times recycle is shown in Fig. 17b. No significant differences in the diffraction peaks were observed, indicating that the composites of 10% $CuBi_2O_4$/CuS micromotorsnanocomposite has a very stable crystal structure. These results suggest that the composites of 10% $CuBi_2O_4$/CuS nanocomposite is very good stability and could be recycled as a photocatalyst.

3.11. Antibacterial Activity

In this study, $CuBi_2O_4$/CuS micromotors bare $CuBi_2O_4$ and CuS were tested (disk diffusion method) for antibacterial activity using Stoplocacous, Kepsila, Bacillus incubations zones are shown Fig.18. The ability of the antibacterial agent to rupture bacterial cells is tested by the disk diffusion method. The presence of an inhibition zone clearly indicates the mechanism of the biocidal action of $CuBi_2O_4$/CuS that involves disrupting the membrane [33]. The high rate of generation of surface oxygen species from $CuBi_2O_4$/CuS leads to the death of the bacteria. The diameter of the inhibition zones results is summarized and presented in Table 2. It is observed that $CuBi_2O_4$ were no antibacterial activity when compared with $CuBi_2O_4$/CuS composites and bare CuS. Therefore, the better antibacterial activity against stoplocacous and bacillus is observed.

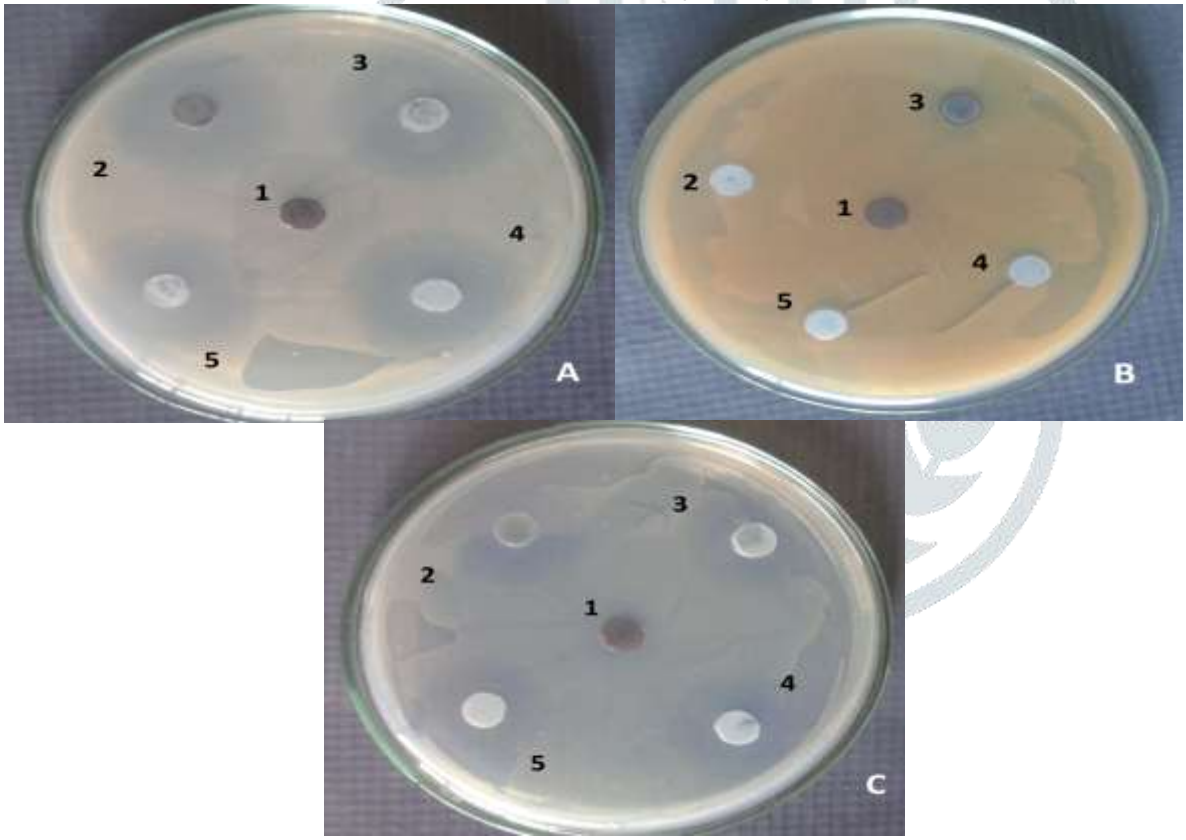

Fig.18. Antibacterial activity of $CuBi_2O_4$, and CuS, $CuBi_2O_4$/CuS micromotors nanocomposite against three pathogenic strains: Stoplocacous, Kepsila, Bacillus shown by the paper disk method.

Table 2. Antibacterial activity of $CuBi_2O_4$, CuS, 1% $CuBi_2O_4$/CuS, 5% $CuBi_2O_4$/CuS, and 10% $CuBi_2O_4$/CuS micromotors nanocomposite.

Bacteria	**Zone Inhibition (mm)**				
	$CuBi_2O_4$	**CuS**	**1 % $CuBi_2O_4$/CuS**	**5% $CuBi_2O_4$/CuS**	**10% $CuBi_2O_4$/CuS**
Stoplocacous	1	16	18	26	20

Kepsila	0	2	2	4	0
Bacilus	2	10	8	20	16

4. Conclusions.

The semiconductor photocatalyst 10%$CuBi_2O_4$/CuS nanocomposite was successfully applied for the degradation and mineralization of p-AP under UV-visible light irradiation. Among the photocatalysts studied, 10% $CuBi_2O_4$/CuS shows superior photocatalytic activity. The PL spectra analysis shows that 10% $CuBi_2O_4$/CuS sample has a lower PL intensity, and the efficient separation of the photogenerated charge carriers which leads to enhanced photocatalytic activities. The optimum reaction conditions are found as follows: pH 6, 10% $CuBi_2O_4$/CuScatalyst dosage350 mg/L, p-AP concentration 15 µM and irradiation time 180 mins. Under the optimum conditions, approximately 84% of p-AP degradation is achieved with the significant reduction in COD (74%) and TOC (68%). The radical trap experiment demonstrates that the hole was the main reactive species for the degradation of pollutants.

Acknowledgements

The author thanks the management of Thiagarajar College and former managementCardamom planters Association College for providing necessary laboratory facilities to carry out this work

References

[1] N-E. Alireza, M. Amiri, Powd. Tech, 235 (2013) 279–288.
[2] M. Sayed, P. Fu, L.A. Shah, H.M. Khan, J. Nisar, M. Ismail, P. Zhang, J.Phy.Chem.A120 (2016) 118–127.
[3] L.G. Kaake, J.J. Jasieniak, R.C. BakusII, G.C. Welch, D.Moses,G.C. Bazan, A.J. Heeger, J.Am.Chem.Soc,134 (2012) 19828–19838.
[4] R-X. Wang, Q.Zhu, W-S. Wang, C-M. Fan, A-W. Xu, New J. Chem, 39 (2015) 4407–4413.
[5] Q. Luo, L. Zhang, X. Chen, O.K. Tan, K.C. Leong, RSC Adv, 6 (2016) 15796–15802.
[6] G. Sharma, Z. Zhao, P. Sarker, B.A. Nail, J. Wang, M.N. Huda, F.E Osterloh, J. Mater. Chem. A, 4 (2016) 2936–2942.
[7] W. Wu, G. L. S. Liang, Y. Chen, L. Shen, H. Zheng, R.Yuan, Y. Hou, L. Wu, J. Catal, 290 (2012) 13–17.
[8] N.R. Manwar, A.A. Chilkalwar,K.K. Nanda, Y.S. Chaudhary, J.Subrt, S.S. Rayalu, N.K.Labhsetwar, ACS Sustainable Chem. Eng, 4 (2016) 2323–2332.
[9] B. Lu, A. Liu, H. Wu, Q. Shen, T. Zhao, J. Wang, Langmuir, 32 (2016) 3085–3094.
[10] Z.Liu, N.Destouches, G.Vitrant, Y.Lefkir, T.Epicier, F.Vocanson, S.Bakhti, Y. Fang, B.Bandyopadhyay, M.Ahmed, J. Phy. Chem. C, 119 (2015) 9496–9505.
[11] F.Motahari, M.R.Mozdianfard, F. Soofivand, S-N. RSC Adv, 4 (2014) 27654–27660.
[12] R.Saleh, N.F.Djaja, Superlat. Microstru, 74 (2014) 217–233.
[13] W.Wu, C.Jiangc, V.A.L.Roy, Nanoscale, 7 (2015) 58–58.
[14] K.Vignesh, R.Priyanka, M.Rajarajan, A.Suganthi, Mate. Sci. Enge: B 178 (2012) 149–157.
[15] H.Fan, H.Li, B.Liu, Y.Lu, T.Xie, D.Wang, ACS Appl. Mater. Inter, 4 (2012) 4853–4857.
[16] C.Karunakaran,S.SakthiRaadha,P.Gomathisankara, P.Vinayagamoorthya, RSC Adv, 3 (2013) 16728–16738.
[17] Y.Deng, Y.Chen, B. Chen, J.Ma, J. Allo.Comp, 559 (2013)116–122.
[18] E.Abdelkadera, L.Nadjiaa, B.Ahmeda, J. King Saud Unive.Sci.27 (2015) 76–91.
[19] J.B.Yoo, H.J.Yoo, H.J.Jung, H.S.Kim, S.Bang, J.Choi, H.Suh, J-H.Lee, J-G. Kim, N.H.Hur, J.Mater.Chem.A 4 (2016) 869–876.
[20] P.Malathy, K.Vignesh, M.Rajarajan, A.Suganthi, Ceram.Internat, 40 (2014)101–107.
[21] K.Vignesh, R.Hariharan, M.Rajarajan, A.Suganthi, Mater. Sci. Semi. Proc,16 (2013) 1521–1530.
[22] R. Cheng, X. Fan, M. Wang, M. Li, J. Tiana, L. Zhang, RSC Adv, 6 (2016) 18990–18995.
[23] Y.Zhoua, S.Fanga, M.Zhoua, G. Wanga, S.Xuea, Z. Lia, S. Xua, C. Yaoa, J. Allo.Compo, 696 (2017) 353–361.
[24] K.Vignesh, A.Suganthi, B.K.Min, M.Kang, App. Surf. Sci, 324 (2015) 652-661.
[25] L.V.Azaroff, M.J.Buerger, MacGraw-Hill, New York, 10 (1958) 252–255.
[26]K.S.W.Sing, D.H.Everett, R.A.W.Haul, L.Moscou, R.A.Pierotti, J.Rouquerol, V.T.Siemieniewska, Pure Appl. Chem, 57 (1985) 603.
[27] S.Selvarajan, A.Suganthi, M.Rajarajan, K.Arunprasath, Powd. Tech, 307 (2017) 203–212.
[28] K.Vignesh, A.Suganthi, B.K.Min, M.Rajarajan, M.Kang, RSC Adva, 5 (2015) 576–585.
[29] R.Satheesh, K.Vignesh, A.Suganthi, M.Rajarajan, J. Environ.Chem.Eng, 2 (2014)1956–1968.
[30] K. Vignesh, M. Rajarajan, A. Suganthi, J. Indu. Eng. Chem, 20 (2014) 3826–3833.
[31] Selvarajan, P. Malathy, A. Suganthi, M. Rajarajan, J. Indu. Eng. Chem, 53 (2017) 201-212.

[32] B. M. Pirzada, N.A. Mir, N. Qutub, O. Mehraj, S. Sabir, M. Muneer, Mater. Sci. Eng. B, 193 (2013) 137–154.
[33] S.Senthilkumar, R.Hariharan, A.Suganthi, M.Ashokkumar, M.Rajarajan, K. Pitchumani, Powd. Tech. 237 (2013) 497–505.